Am J Transl Res 2024;16(4):1081-1101
www.ajtr.org /ISSN:1943-8141/AJTR0154654

Original Article

Integration of bulk RNA-seq and single-cell RNA-seq constructs: a cancer-associated fibroblasts-related signature to predict prognosis and therapeutic response in clear cell renal cell carcinoma

Jiating Cui[1,2], Xuanzhen Zhou[1], Shuben Sun[1,3,4]

[1]Department of Urology, The First Affiliated Hospital of Ningbo University, Ningbo 315020, Zhejiang, China; [2]Health Science Center, Ningbo University, Ningbo 315211, Zhejiang, China; [3]Ningbo Clinical Research Centre for Urological Disease, The First Affiliated Hospital of Ningbo University, Ningbo 315010, Zhejiang, China; [4]Zhejiang Engineering Research Center of Innovative Technologies and Diagnostic and Therapeutic Equipment for Urinary System Diseases, Ningbo 315010, Zhejiang, China

Received November 28, 2023; Accepted April 8, 2024; Epub April 15, 2024; Published April 30, 2024

Abstract: Background: Clear cell renal cell carcinoma (ccRCC) is a common and aggressive renal cancer with high mortality when metastasized. Cancer-associated fibroblasts (CAFs) are pivotal in ccRCC evolution; however, their significance in forecasting prognosis and guiding therapy is undetermined. Method: We used Weighted Correlation Network Analysis to identify modules correlated with CAFs in bulk RNA-seq data. We also screened fibroblast marker genes in single-cell RNA-seq data and upregulated genes in TCGA tumor samples and defined genes identified in all three analyses as CAFs-related genes (CRGs). We extracted a CRG signature using Least Absolute Shrinkage and Selection Operator analysis and investigated its biological mechanisms by combining Gene Set Enrichment Analysis and the AUCell algorithm. The Tumor Immune Dysfunction and Exclusion algorithm and the IMvigor 210 dataset were employed to assess the signature's capability to predict immunotherapeutic responses. Additionally, we analyzed the relationship between the signature and the IC_{50} of targeted agents. In vitro validation confirmed the relative mRNA expression of the CRGs and the function of CERCAM. Results: The CRG signature was anchored on six genes: CERCAM, TMEM132A, TIMP1, P4HA3, FKBP10, and CEBPB. Kaplan-Meier analysis indicated that patients with high expression of the signature experienced poorer survival than those with low expression. Furthermore, immunotherapy was more effective in patients with low signature expression. In vitro assays revealed CERCAM silencing led to a substantial reduction in the proliferative and migratory capacities of ccRCC cell lines. Conclusion: Our CRG signature holds promise in forecasting prognosis and guiding personalized treatment for patients with ccRCC.

Keywords: Cancer-associated fibroblasts, clear cell renal cell carcinoma, prognosis, immunotherapy, tumor microenvironment

Introduction

Renal cell carcinoma (RCC) ranks as the third most prevalent urological malignancy, representing 2.2% of all cancer diagnoses [1]. In 2020, over 430,000 new RCC cases were recorded worldwide, accompanied by 170,000 fatalities. Clear cell renal cell carcinoma (ccRCC) is the most predominant histologic variant of RCC, accounting for at least 70% of all RCC diagnoses [2]. Tragically, about 30% of patients with ccRCC face recurrence or metastases after undergoing radical nephrectomy or similar treatment. This recurrence leads to an increase in mortality rates [3, 4]. Current treatment modalities, including hormonal therapy (e.g., tamoxifen, primostat, or medroxyprogesterone), chemotherapy (e.g., 5-fluorouracil combined with doxorubicin and gemcitabine), and radiotherapy, have not resulted in significant improvement in survival or quality of life for these patients [5].

The tumor microenvironment (TME) exerts a significant influence on the proliferation, advancement, and spread of tumor cells. Within

the multifaceted ensemble of stromal cells constituting the TME, cancer-associated fibroblasts (CAFs) are paramount contributors. The significant functional heterogeneity of CAFs can be attributed to their diverse cellular origins, which include normal fibroblasts, bone marrow-derived mesenchymal stem cells, endothelial cells, adipocytes, epithelial cells, pericytes, and smooth muscle cells [6]. Although normal human fibroblasts inhibit cancer cell growth, CAFs typically show tumorigenic proliferation, invasion, release of angiogenic growth factors, extracellular matrix (ECM) remodeling, epithelial-mesenchymal transition (EMT), and induction of inflammation and antitumor immunity [7-9]. CAFs not only activate oxidative stress pathways and autophagy mechanisms, which benefit the metabolism of cancer cells and provide essential nutrients [10-12], but also contribute to the development of an immune-cold tumor phenotype [13]. This is achieved through their ability to directly inhibit T cell infiltration and activation, as well as to promote the recruitment of immunosuppressive cell types. Traditional targeted treatments have their limitations. However, there is growing recognition of the benefit that can come from combining these treatments with immune therapies that target CAFs [14]. This emphasizes the need to identify a novel CAF-related gene (CRG) signature.

Among urological malignancies, there is mounting evidence that highlights the potent prognostic capability of CRG signatures in bladder and prostate cancers [15, 16]. However, the role and mechanism of the CRG signature in ccRCC are still unclear. This gap signifies an urgent need for deeper insight into the multifaceted roles and underlying mechanisms of CAFs in ccRCC.

Bulk RNA sequencing (RNA-seq) provides data on average gene expression levels, which are suitable for in-depth analyses of gene expression profiles. Previous studies have acknowledged Weighted Gene Co-expression Network Analysis (WGCNA) as a powerful tool for pinpointing CRGs within bulk RNA-seq data [17]. Although the sequencing depth of single-cell RNA sequencing (scRNA-seq) may not be as comprehensive as that of bulk RNA-seq, the single-cell approach provides more detailed biological insight. This enhanced granularity is particularly effective in unveiling the diverse heterogeneity of CAFs across a wide array of cancer types [18-21].

In this study, we analyzed data from bulk RNA-seq and scRNA-seq independently to identify genes with CAF-specific expression. Genes that were consistently identified by both methods were considered CRGs. This approach ensured the compatibility and stability of results derived from different sequencing techniques, enabling a comprehensive bioinformatic exploration of the CRG signature and further substantiation through in vitro validation. We aimed to gauge the prognostic relevance of a CAF score based on CRG expression for ccRCC patients and to refine therapeutic strategies based on our insights.

Materials and methods

Sample data acquisition and standardization

We obtained integrated bulk RNA-seq data and clinical information for the TCGA-KIRC dataset (533 tumor and 72 normal tissues) and the E-MTAB-1980 dataset (101 tumor tissues) from the ArrayExpress database [22]. Before proceeding with external validation, we used the "sva" package (ver. 3.44.0) to mitigate batch effects between the two datasets [23]. Additionally, we acquired the GSE111360 scRNA-seq dataset, which comprises 23,130 ccRCC cells obtained from two ccRCC samples, from the GEO database [24]. We used the IMvigor210 dataset, which includes 348 patients with various tumor types receiving anti-PD-L1 therapy, to validate the CRG signature's performance in predicting immunotherapeutic response.

Identification of CAFs-related module eigengenes by WGCNA

The "MCPcounter" R package (ver. 1.2.0) was utilized to estimate the proportions of immune and stromal cell infiltration [25]. For the TCGA-KIRC dataset, we employed WGCNA (ver. 1.72-1) to create a co-expression network. To achieve a scale-free network, we selected an appropriate soft threshold power, represented as β. Using Topological Overlap Matrix analysis, we clustered the adjacency matrix from the bulk RNA-seq data. A Dynamic Tree Cut algorithm allowed us to discover differential modules in the hierarchical clustering diagram, with

each module containing over 30 genes. Finally, we calculated the Pearson correlation coefficients and corresponding *p*-values to assess the correlation strengths between module eigengenes and the proportions of immune and stromal cells.

ScRNA-seq data analysis

For analysis of 23,130 ccRCC cells from two patients, we employed the Seurat package (ver. 4.3.0.1). Cells marked with fewer than 50 genes were classified as low-quality or empty droplets and were subsequently removed. Additionally, cells containing more than 5% mitochondrial gene content were deemed damaged and were excluded. Next, after normalizing the gene expression using the NormalizeData function in Seurat, we pinpointed the 3,000 most variable genes using Principal Component Analysis (PCA). Using the first 25 principal components, we identified clusters at 0.5 resolution and visualized them by Uniform Manifold Approximation and Projection (UMAP). We used the FindAllMarkers function in Seurat to discover marker genes for individual cell clusters, with a log2-fold change above 0.25 and an adjusted *p*-value below 0.05 as the selection criteria. For cell type annotation, we employed the SingleR package (ver. 1.10.0) with BlueprintEncodeData as the reference set. To ensure accuracy, fibroblasts were manually annotated using COL1A2 as the marker gene.

Identification of CRGs and enrichment analysis

Differential analysis was performed on count data from 72 normal samples and 533 tumor samples using the "DESeq2" R package (ver. 1.36.0). Genes exhibiting a $\log_2$-fold change greater than 0.25 and an adjusted *p*-value less than 0.05 were classified as differentially expressed genes (DEGs). Volcano plots were used to display the results of the differential analysis. We used an intersection strategy to identify CRGs that were common to the module eigengenes selected by the WGCNA of the TCGA-KIRC dataset, the upregulated DEGs selected in the differential analysis of the TCGA-KIRC dataset, and the fibroblast marker genes selected by the scRNA-seq analysis. To explore the biologic significance of the CRGs, we performed Kyoto Encyclopedia of Genes and Genomes (KEGG) and Gene Ontology (GO) analyses with the "clusterProfiler" R package (ver. 4.6.1). An adjusted *p*-value less than 0.05 was considered significant for the results of the enrichment analysis.

Development and validation of a predictive gene signature

Using the TCGA-KIRC dataset as a training cohort, for the identified hub genes, we performed a univariate Cox regression survival analysis to identify prognostic CRGs, applying a significance threshold of $P < 0.05$. To mitigate overfitting and optimize the model performance, we conducted Least Absolute Shrinkage and Selection Operator (LASSO) Cox regression analysis with 10-fold cross-validation and 1000 iterations. We used the "glmnet" package (ver. 4.1-6) to perform this analysis on the identified genes. Subsequently, the CAF score was calculated by the following method:

$$CAFs\ Score = \sum_{i=1}^{n} Coef(i) * Expr(i)$$

According to the median CAF score, we classified the 533 ccRCC samples into two categories: low-CAF and high-CAF groups. Scatter plots elucidated the correlation between CAF scores and survival status. Both PCA and t-Distributed Stochastic Neighbor Embedding (t-SNE) were employed to evaluate the capability of the risk model to distinguish between the low-CAF and high-CAF groups. To assess the differential overall survival between the two groups, we conducted a survival analysis utilizing Kaplan-Meier curves and log-rank tests. We also plotted time-dependent Receiver Operating Characteristic (ROC) curves to gauge the model's prognostic accuracy. For further validation, we also applied the CAF risk model to the E-MTAB-1980 dataset.

Gene set enrichment analysis

Using the TCGA-KIRC dataset, we conducted a Gene Set Enrichment Analysis (GSEA) of the high-CAF group. Reference gene sets for this analysis were sourced from KEGG and Hallmark annotations, using files "c2.cp.kegg.Hs.symbols.gmt" and "h.all.v2023.1.Hs.symbols.gmt" from MSigDB. In the GSE111360 dataset, we scored each cell based on the KEGG and Hallmark annotations using the "AUCell" package (ver. 1.18.1). The resulting enrichment analyses were subsequently visualized.

Table 1. Primer sequences used in qPCR

Primer Name	Forward Sequence (5'→3')	Reverse Sequence (5'→3')
β-actin	CATGTACGTTGCTATCCAGGC	CTCCTTAATGTCACGCACGAT
CERCAM	CACATCCCAACTACACTTGGC	ATGTACCCATAACGGTGCTCA
TMEM132A	AACTGTCTGAGTTCCTATGGGT	CAGTGGGATAAGGGCTCTGAT
TIMP1	AGAGTGTCTGCGGATACTTCC	CCAACAGTGTAGGTCTTGGTG
P4HA3	GCTGCGGGACCTGACTAGA	CAAGCAGAGGGTTAGCCACAG
FKBP10	TACCACTACAACGGCACTTTTG	AGAACCACATCGAAGTAGAGGG
CEBPB	CTTCAGCCCGTACCTGGAG	GGAGAGGAAGTCGTGGTGC

Analysis of clinicopathological features correlations and development of a nomogram

For the TCGA-KIRC dataset, we aimed to examine the correlation between the CAFs scores and clinicopathological features (gender, age, clinical stage, and T/M/N classification). To compare the differences in CAF scores between different subgroups, Student's t-tests were employed. We calculated the *p*-values between each pair of independent subgroups to determinewhether the differences between them were significant. Subsequently, univariate and multivariate Cox regression analyses were performed. To enhance our capability to predict clinical outcomes, we constructed a nomogram that factors in age, gender, clinical stage, T/M/N stage, and the CRG signature. Subsequently, we evaluated the robustness and precision of the nomogram with a calibration plot and an ROC curve analysis.

Immune landscape and immunotherapy analyses

We used the ESTIMATE algorithm to analyze the immune landscape of the TCGA-KIRC dataset and determine the Immune Score and the Stromal Score. Subsequently, we employed these values to compute the ESTIMATE Score, which serves as an indicator of tumor purity. Using the Proportion of Immune and Cancer Cell (EPIC) deconvolution algorithm, we determined the proportions of five immune-cell subtypes and two stromal-cell subtypes. We also used Pearson correlation coefficients to examine the relationships between the CAF scores and factors such as immune-checkpoint gene expression levels and immune and stromal cell proportions, as identified by the EPIC algorithm. Using the "gsva" R package (ver. 1.46.0), we conducted single-sample GSEA to obtain activity scores for immune-related pathways. To predict responses to immune-checkpoint blockade therapies, including anti-PD1 and anti-CTLA4, we assigned scores to each tumor sample using the Tumor Immune Dysfunction and Exclusion (TIDE) algorithm. We then evaluated differences in immunotherapy efficacy between the high-CAF and low-CAF groups by Student t-test and χ^2 test, and we assessed the predictive accuracy of our CRG signature by ROC curve analysis. For additional insight into survival outcomes and the potential efficacy of anti-PD-L1 treatment, we referenced the IMvigor 210 cohort.

Drug sensitivity predictions

The R package OncoPredict (ver. 0.2) is designed to predict drug responses. Using this package, we conducted Student t-tests to explore the associations between the high-CAF and low-CAF groups and their IC_{50} values for molecular targeting drugs.

Cell culture and RT-qPCR

The renal epithelial cell line HK-2 and the ccRCC lines 786-O and A-498 were sourced from Procell (Wuhan, China), cultured in DMEM high-glucose medium supplemented with 10% fetal bovine serum (both from Gibco, CA, USA), and maintained at 37°C in a 5% CO_2 atmosphere. Total RNA was isolated using TRIzol Reagent (Life, CA, USA). The isolated RNA was reverse transcribed into cDNA using HiScript II Reverse Transcriptase, and qPCR was performed using Taq Pro DNA Polymerase (both from Vazyme, Nanjing, China). Relative mRNA expression levels were quantified using the $2^{-\Delta\Delta Ct}$ method after normalization to reference genes. The experiment used the primer sequences shown in **Table 1**.

Cell transfection

Before transfection, 5×10^5 cells from the 786-O and A498 cell lines were plated in each well of six-well plates and incubated overnight. Once the tumor cells reached 70-80% confluency, they were transfected using a mixture of siRNA or negative control siRNA (Genepharma, Shanghai, China) in conjunction with Lipofectamine 2000 (Invitrogen, CA, USA) in Opti-

MEM medium (Gibco, CA, USA). After 5 hours of transfection incubation, the cells were switched to complete medium for continued culture. After 48 hours, the cells were ready for subsequent experiments.

CCK-8 assay

After the transfection procedure, cellular aliquots were systematically seeded into 96-well plates at a density of 2×10^4 cells per well. Following the standardized protocol provided by the CCK-8 manufacturer (Beyotime, Shanghai, China), we pipetted 10 μl CCK-8 solution into each designated well. Subsequent absorbance readings were taken at 450 nm at specified intervals - 0, 24, 48, and 72 hours - using a high-precision microplate reader to accurately assess cellular viability.

Colony-formation assay

In six-well plates, 500 transfected cells were seeded per well and incubated in complete medium for 7 days. Following incubation, the cells were preserved using 4.0% paraformaldehyde and stained with 0.1% crystal violet (both sourced from Solarbio, Beijing, China). The fixation and staining durations were 15 minutes and 10 minutes, respectively. After staining, any residual dye was rinsed off using distilled water.

Wound-healing assay

In six-well plates, 5×10^5 transfected cells were plated into each well and cultured overnight in complete medium. A cell-free zone in the monolayer was created using a 200 μl pipette tip. The plate was gently rinsed twice with PBS to eliminate detached cells and then cultured in Opti-MEM medium to minimize cell proliferation and focus on migration. Cell migration was evaluated using a microscope at 40 × magnification by capturing images at 0 and 24 hours.

Statistical analyses

Data were processed and visualized with GraphPad Prism 8 (ver. 8.0.2) and R (ver. 4.2.2). Student t-test was employed to compare data between two groups. Kaplan-Meier curves accompanied by log-rank tests were used to compare survival between groups. Additionally, Pearson correlation analysis was applied to assess linear relationships between continuous variables. The χ^2 test was used to compare proportions between categorical groups. A p-value ≤ 0.05 was deemed to indicate significance.

Results

Identification of a gene module associated with CAF infiltration

Gene co-expression analysis was conducted, and Pearson correlations between co-expression modules and tumor infiltration of eight types of immune cells and two types of stromal cells were assessed. For the TCGA-KIRC dataset, a soft threshold power (β) of 6 was determined to be optimal for establishing a scale-free topological network with an R^2 value of 0.86 (**Figure 1A**). The resulting cluster dendrogram identified eight gene modules that exhibited similarities, delineated at a cut height of 0.2 (**Figure 1B**, **1C**). Remarkably, the pink module demonstrated the strongest association with CAFs infiltration, with a correlation coefficient of 0.96 and a significance level of $P < 0.001$ (**Figure 1D**). Following this analysis, we focused our investigations on the 314 phenotypic genes identified within the pink module.

Discovery and enrichment analysis of CAFs-related genes

Using the Seurat package for quality control, 23,088 high-quality cells were isolated from the single-cell dataset. These cells were subjected to UMAP for dimensionality reduction, resulting in 24 distinct clusters (**Figure 2A**). The DEGs for each cluster were computed and compared with the annotated gene set, which identified eight cell types: T cells, Mono/Macrophages, NK cells, B cells, fibroblasts, plasma cells, dendritic cells, and mast cells (**Figure 2B**). Following this, a total of 3234 fibroblast marker genes were identified. A volcano plot displayed 7711 upregulated DEGs and 5359 downregulated DEGs (**Figure 2C**). The intersection of marker genes, module eigengenes, and upregulated DEGs was visualized in a Venn diagram (**Figure 2D**). From this intersection, we identified 29 common genes. These intersecting genes were subsequently defined as CRGs. To further enrich our understanding of the CRGs, we subjected them to rigorous

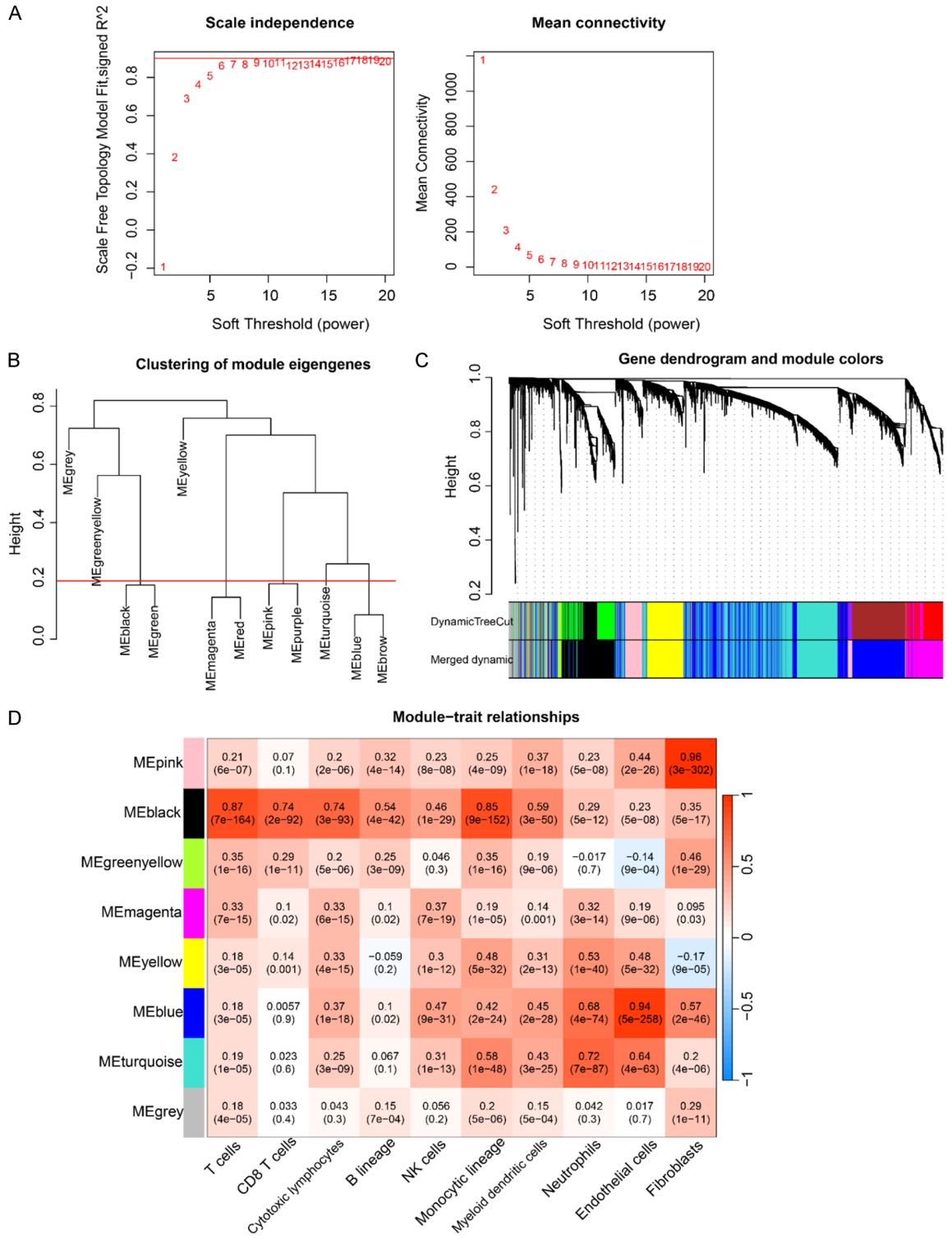

Figure 1. Co-expression network constructed by WGCNA. A. Analysis of the TCGA-KIRC dataset identified an optimal soft threshold power (β) of 6 for achieving a scale-free topological network. B. The cluster dendrogram identified 12 preliminary co-expression modules. C. Among these, similarly expressed modules were consolidated, resulting in a final set of eight distinct co-expression modules. D. A heatmap depicting correlations between the derived modules and specific cell types, with correlation coefficients and accompanying *p*-values displayed within each grid. WGCNA: Weighted Gene Co-expression Network Analysis.

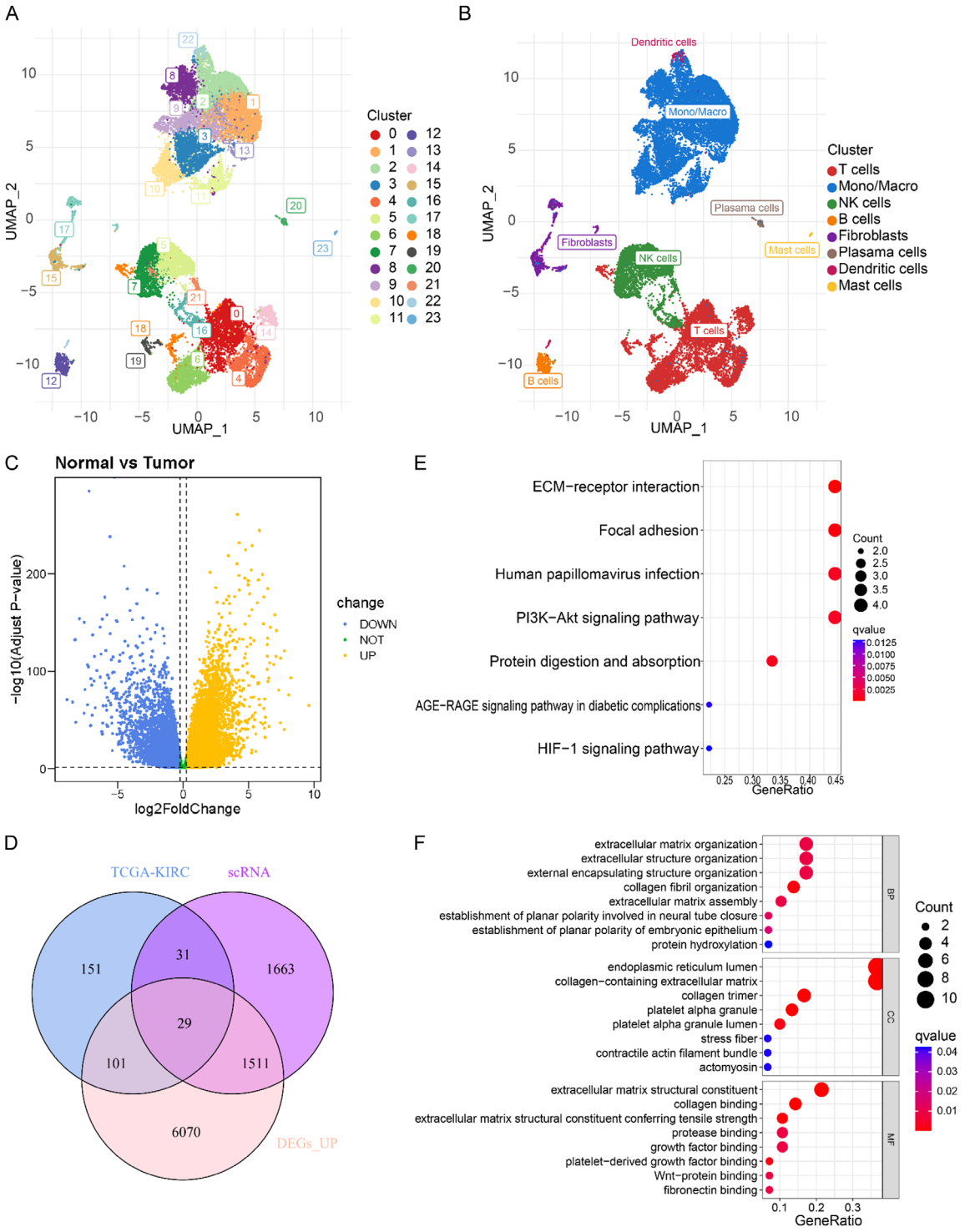

Figure 2. Identification and functional analysis of CAF-associated genes. (A) UMAP of GSE111360 clustered the cells into 24 clusters. (B) The 24 clusters were annotated as eight cell types. (C) Volcano plot of DEGs between tumor and normal tissues in the TCGA-KIRC dataset, with the selection criteria of a $\log_2$-fold change greater than 0.25 and an adjusted *p*-value less than 0.05. (D) Venn plot displays the intersection of marker genes, module eigengenes, and upregulated DEGs. (E) KEGG pathway analysis and (F) GO analysis of the 29 CRGs. CAFs: cancer-associated fibroblasts; UMAP: Uniform Manifold Approximation and Projection; DEGs: differentially expressed genes; KEGG: Kyoto Encyclopedia of Genes and Genomes; GO: Gene Ontology; CRGs: CAFs-related genes; BP: Biological Process; CC: Cellular Component; MF: Molecular Function.

analyses using both the KEGG and the GO methodologies. The KEGG analysis indicated primary involvements in pathways like ECM-receptor interaction, focal adhesion, and PI3K-Akt signaling (**Figure 2E**). The GO analysis revealed predominant associations with ECM organization and extracellular structure organization for Biological Process (BP), collagen-containing ECM and endoplasmic reticulum lumen for Cellular Components (CC), and ECM structural constituent for Molecular Function (MF) (**Figure 2F**).

Construction and validation of the CRG signature

Using the TCGA-KIRC training dataset, we sought to understand the prognostic value of CAFs in ccRCC. We began by extracting the CRG expression data and merging the data with information on patient survival. We identified 22 prognosis-related genes using univariate regression analysis (**Figure 3A**). To optimize the gene signature for overall survival prediction, we utilized LASSO regression analysis, narrowing our focus to a subset of six prognosis-related CRGs (**Figure 3B**, **3C**). The model derived from these genes is expressed as the CAFs score = RNA-seq of CERCAM × 0.0559 + RNA-seq of TMEM132A × 0.0827 + RNA-seq of TIMP1 × 0.1135 + RNA-seq of P4HA3 × 0.0371 + RNA-seq of FKBP10 × 0.0556 + RNA-seq of CEBPB × 0.0878. Using the median CAFs score as a threshold, patients within the TCGA-KIRC training cohort and the E-MTAB-1980 test cohort were categorized into high-CAF and low-CAF groups. For both cohorts, the heatmap for CERCAM, TMEM132A, TIMP1, P4HA3, FKBP10, and CEBPB; the distribution of CAFs scores; and the survival status of patients are displayed, depicting a trend of decreasing survival time with increasing CAF score (**Figure 3D**, **3E**). Employing PCA and t-SNE plots, we showcased the robust discriminatory capability of our CRG signature in differentiating between the two groups across the training (**Figure 3F**, **3G**) and test (**Figure 3H**, **3I**) cohorts. Kaplan-Meier survival curves exhibited notable distinctions in prognosis between the two groups in both the training cohort (**Figure 3J**) and the test cohort (**Figure 3L**), with the high-CAF groups manifesting poorer outcomes. Additionally, the ROC curves reflected the strong prognostic performance of the CRG signature. The AUC values were 0.686, 0.630, and 0.630 at 1, 3, and 5 years, respectively, for the training cohort (**Figure 3K**) and 0.636, 0.643, and 0.684 at the same time points for the test cohort (**Figure 3M**).

Gene set enrichment analysis

To elucidate the pathway and gene set enrichment of the CRG signature, GSEA was carried out using the TCGA-KIRC dataset. Notably enriched KEGG signaling pathways in the high-CAF group included cell cycle, cancer pathways, ECM-receptor interaction, TGF-β signaling, focal adhesion, cytokine-cytokine receptor interaction, WnT signaling, and hedgehog signaling (**Figure 4A**). Similarly, prominent hallmark gene sets in this group encompassed EMT, inflammatory response, hypoxia, IL6-Jak-Stat3 signaling, upregulated KRAS signaling, glycolysis, apoptosis, and TNF-α signaling by NF-κB (**Figure 4B**). Using the AUCell package for enrichment analysis of KEGG and Hallmark gene sets in the GSE111360 dataset, we observed that pathways such as ECM-receptor interaction, EMT, hypoxia, and glycolysis exhibited higher AUC scores in fibroblasts (cluster 15 and 17) compared to other cell types (**Figure 4C**, **4D**). These findings suggest that the CRG signature might channel these pathways through fibroblasts, accelerating ccRCC progression, invasion, and metastasis.

Clinicopathologic feature correlations and construction of a nomogram

To comprehensively analyze the CRG signature in the TCGA-KIRC dataset, we investigated the relationships between CAF scores and various clinicopathologic characteristics (**Figure 5A**). Our analysis revealed that patients with higher CAF scores often had more advanced T/M/N stage and clinical stage. Interestingly, we observed statistically significant differences in CAF scores among gender subgroups. We employed univariate and multivariate Cox analyses sequentially. The results demonstrated that CRG signature served as an independent prognostic factor (**Figure 5B**, **5C**). We then constructed a nomogram incorporating the CRG signature with other clinicopathologic features to predict the 1-, 3-, and 5-year overall survival rates of ccRCC patients (**Figure 5D**). We also generated calibration plots, confirming the predictive reliability of our nomogram

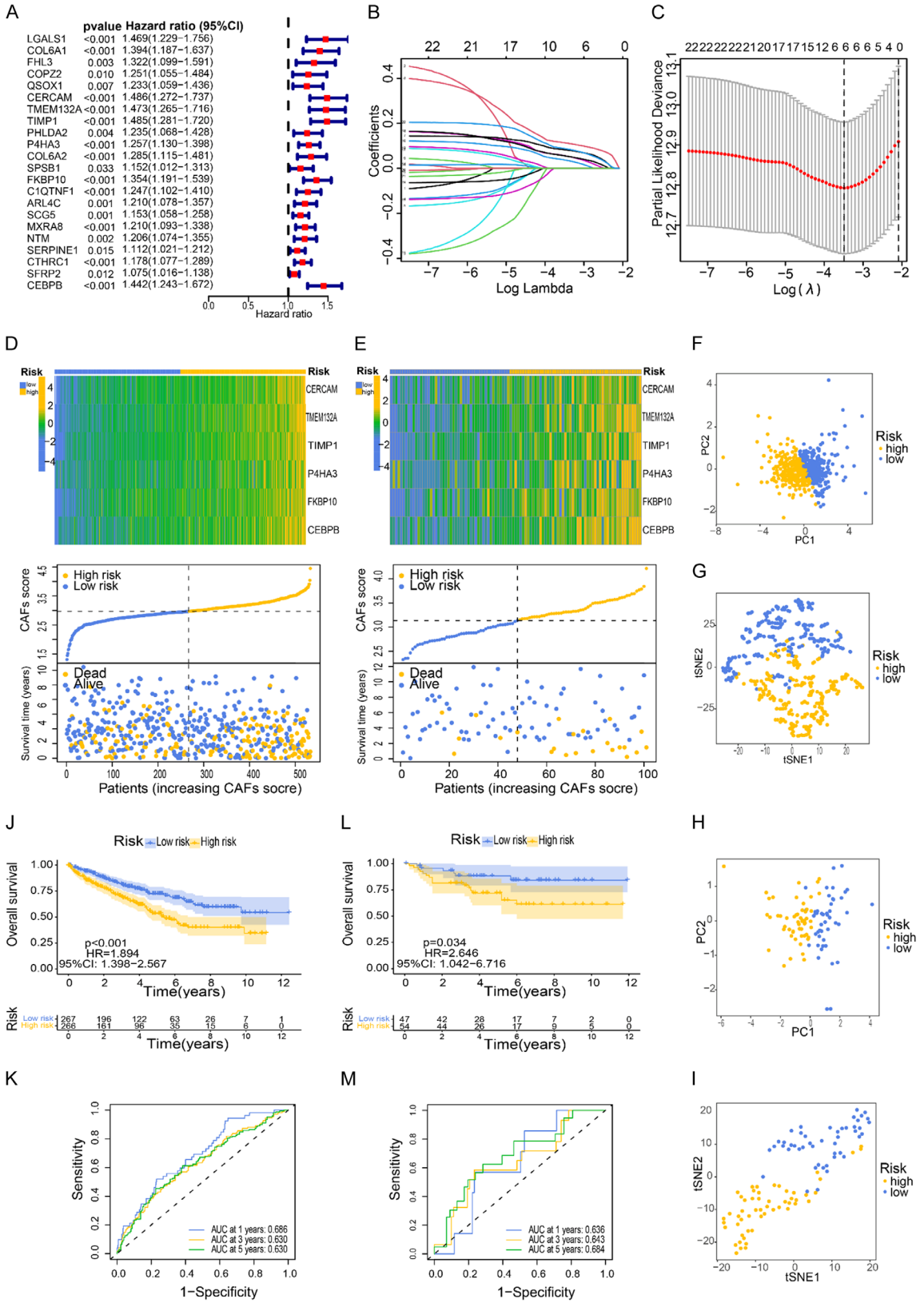

Figure 3. Development and validation of the CRG signature. (A) Univariate Cox analysis of hub genes in the training cohort. (B) Coefficients derived from the LASSO regression model. (C) Determination of the optimal λ value through 10-fold cross-validation. In the training (D) and test (E) cohorts, the heatmap of CERCAM, TMEM132A, TIMP1,

P4HA3, FKBP10, and CEBPB, the distribution of CAF scores, and the survival status of patients are shown. The performance of CAF scores in distinguishing individuals from different groups in the training (F, G) and test (H, I) cohorts. Kaplan-Meier survival analysis for the training (J) and test (L) cohorts. Time-dependent ROC curves in the training (K) and test (M) cohorts. CRG: CAFs-related gene; CAFs: cancer-associated fibroblasts; LASSO: Least Absolute Shrinkage and Selection Operator; ROC: Receiver Operating Characteristic; CI: confidence interval.

(**Figure 5E**). Furthermore, we used ROC curves to assess the prognostic accuracy of the nomogram as well as that of other features (**Figure 5F**). Notably, the AUC value reached 0.906, showing that the nomogram offered superior prognostic accuracy compared to other features.

Analysis of immune landscape and immunotherapy response

In the TCGA-KIRC dataset, significant differences in Immune, Stromal, and ESTIMATE scores were observed between the high-CAF and low-CAF groups (**Figure 6A-D**). Specifically, the high-CAF group showed increased values for these scores and a decreased Tumor Purity score. To prevent overfitting, we utilized the EPIC algorithm instead of the MCPcounter algorithm to calculate the proportions of different types of cells within the TME (**Figure 6G**). Our analysis revealed that compared to the low-CAs group, the high-CAF group exhibited significantly higher fractions of CAFs, endothelial cells, and macrophages. Conversely, the proportions of NK cells, CD8 T cells, and CD4 T cells were markedly lower in the high-CAF group (**Figure 6E**). We also uncovered a strong positive correlation between the CAF scores and the proportion of fibroblasts, as illustrated in **Figure 6H**. Additionally, immune-related pathway activities such as APC co-stimulation, CCR, checkpoint, parainflammation, T cell co-stimulation, type I IFN response, and type II IFN response were more active in the high-CAF group (**Figure 6F**). Positive correlations were also observed between the CAF scores and the expression of most immune-checkpoint genes (**Figure 6I**).

We applied the TIDE algorithm to predict the response to immunotherapies, specifically anti-PD-1 and anti-CTLA-4, in ccRCC patients from the TCGA-KIRC cohort. Our findings showed that the high-CAF group exhibited a greater potential for immune escape than the low-CAF group, suggesting a diminished likelihood of favorable immunotherapeutic response (**Figure 7A**). This was further substantiated by the significantly higher non-response rate to immunotherapy in the high-CAF group compared to the low-CAF group (**Figure 7B**). The efficacy of our model for predicting immunotherapy response was validated by the ROC curve, which yielded an AUC of 0.785 (95% CI: 0.746-0.823; **Figure 7C**). Turning our attention to the IMvigor210 dataset, we investigated the response to anti-PD-L1 immunotherapy. In this cohort, the high-CAF group demonstrated a poorer prognosis than the low-CAF group (**Figure 7D**). Intriguingly, those with stable disease or progressive disease (SD/PD) registered markedly higher CAF scores compared with individuals with a complete or partial response (CR/PR; **Figure 7E**). The predictive accuracy of our model was evident from the ROC curve, which reported an AUC of 0.598 (95% CI: 0.524-0.669; **Figure 7F**).

Drug sensitivity analysis

In the TCGA-KIRC cohort, we evaluated the sensitivity of ccRCC patients to various targeted agents. We observed significant differences in sensitivity between the high-CAF and low-CAF groups. As shown in **Figure 8**, patients in the high-CAF group were less sensitive to erlotinib, gefitinib, sinularin, and sorafenib but more sensitive to buparlisib, dactolisib, dasatinib, foretinib, and trametinib.

Verification of differential expression for the CRGs

To further validate the CRGs, we performed RT-qPCR assays for CERCAM, TMEM132A, TIMP1, P4HA3, FKBP10, and CEBPB in the HK-2, 786-O, and A498 cell lines. As shown in **Figure 9A**, both 786-O cells and A498 cells showed markedly elevated mRNA expression of these genes compared to HK-2 cells.

Knockdown of CERCAM suppressed the proliferation and migration of 786-O cells and A498 cells

First, we measured the mRNA expression levels of CERCAM in 786-O and A498 cells post-transfection with siRNA using RT-qPCR to confirm

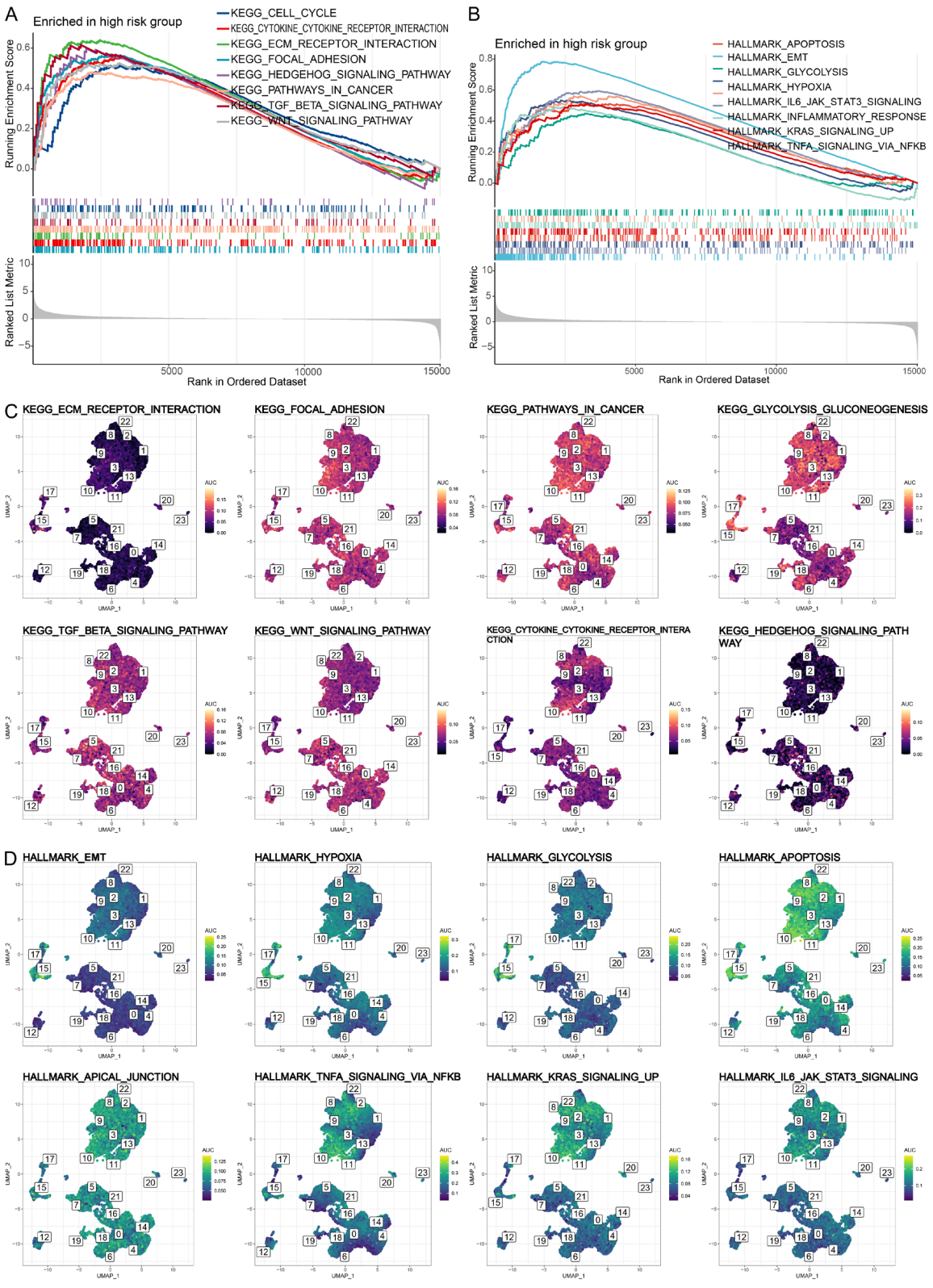

Figure 4. GSEA of the TCGA-KIRC and GSE111360 datasets. A, B. Analysis of KEGG signaling pathways and Hallmark gene sets in the high-CAF group. C, D. The activity levels of KEGG signaling pathways and Hallmark gene sets in various cell clusters. CAFs: cancer-associated fibroblasts; GSEA: Gene Set Enrichment Analysis; KEGG: Kyoto Encyclopedia of Genes and Genomes.; CAFs: cancer-associated fibroblasts.

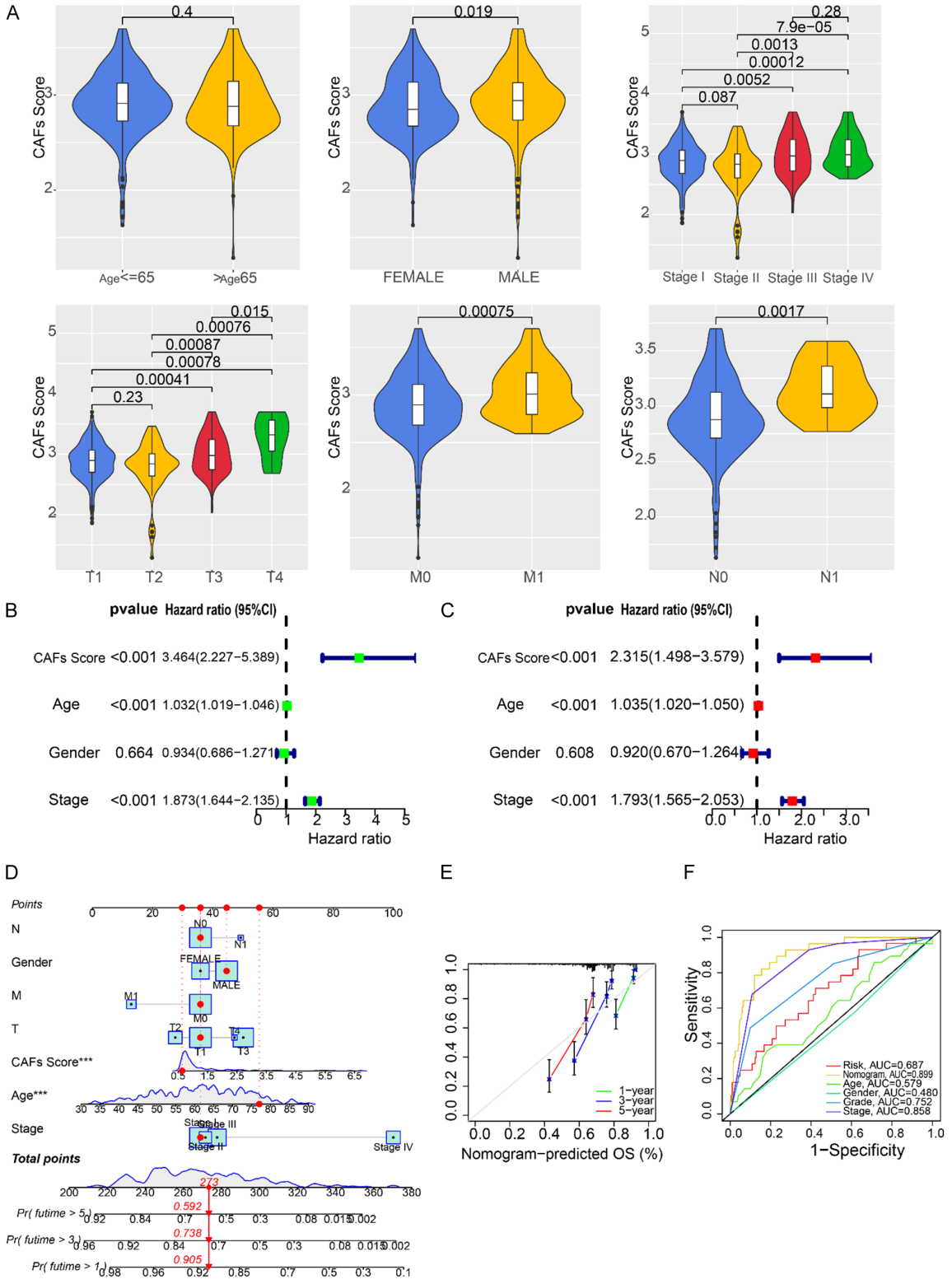

Figure 5. Differences in CAF scores based on clinicopathologic features and construction of a nomogram. (A) Relationship between CAF scores and various clinicopathological characteristics. (B) Univariate and (C) Multivariate Cox analyses. (D) A nomogram predicting the overall survival of ccRCC patients. (E) Calibration curve for validating the predictive reliability for overall survival. (F) ROC curves employed to assess the prognostic accuracy of the nomogram compared with that of other features. ***P < 0.001. CAFs: cancer-associated fibroblasts; ROC: Receiver Operating Characteristic; OS: overall survival; CI: confidence interval.

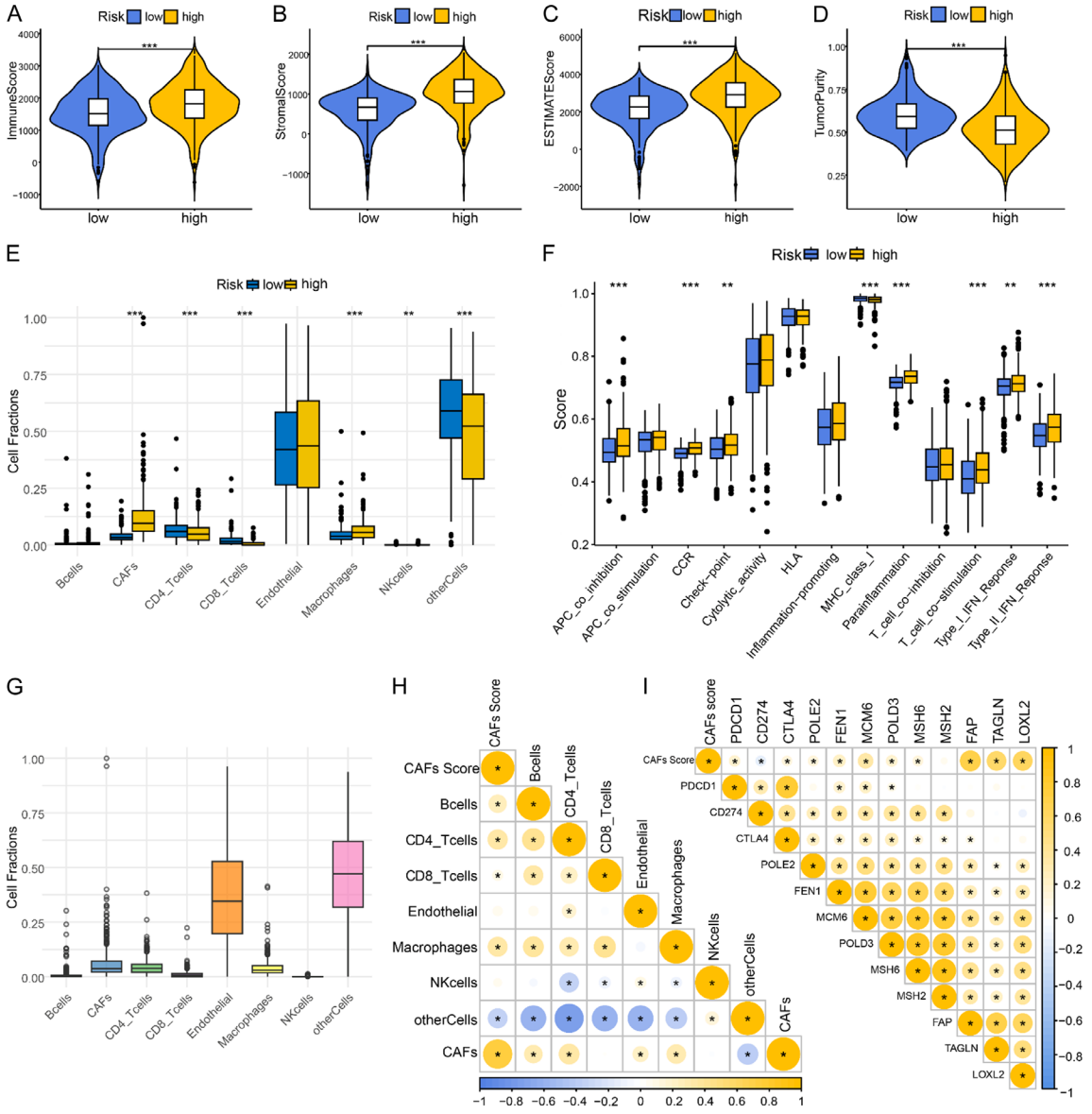

Figure 6. Infiltration of immune and stromal cells in high-CAF and low-CAF groups. A-D. Differences between groups in TME scores. E. Differences between groups in five immune-cell subtypes and two stromal-cell subtypes. F. Differences between groups in immune-related pathway activity. G. The proportion of different types of cells within the TME. H. Correlations between different cell types and CAF scores. I. Correlations between immune-checkpoint gene expression levels and CAF scores. *P < 0.05; **P < 0.01; ***P < 0.001. CAFs: cancer-associated fibroblasts; TME: tumor microenvironment.

the efficiency of CERCAM knockdown by the siRNA (**Figure 9B**). Assessments of cell proliferation in siRNA-transfected 786-O and A498 cells were conducted using CCK-8 and colony-formation assays. Our findings underscore that CERCAM augments the proliferative potential of these cells, as illustrated in **Figure 9C** and **9D**. Additionally, wound-healing assays revealed that downregulation of CERCAM considerably reduced the migratory capabilities of the aforementioned cell lines (**Figure 9E**, **9F**).

Discussion

Clear cell renal carcinoma is the predominant subtype of kidney cancer that originates from renal tubular epithelial cells within the parenchyma. Although patients with early-stage kidney cancer can benefit from surgical intervention, many patients present at advanced stages of the disease, when the prognosis is worse [26]. Recent therapeutic paradigms emphasize combined targeted therapy and

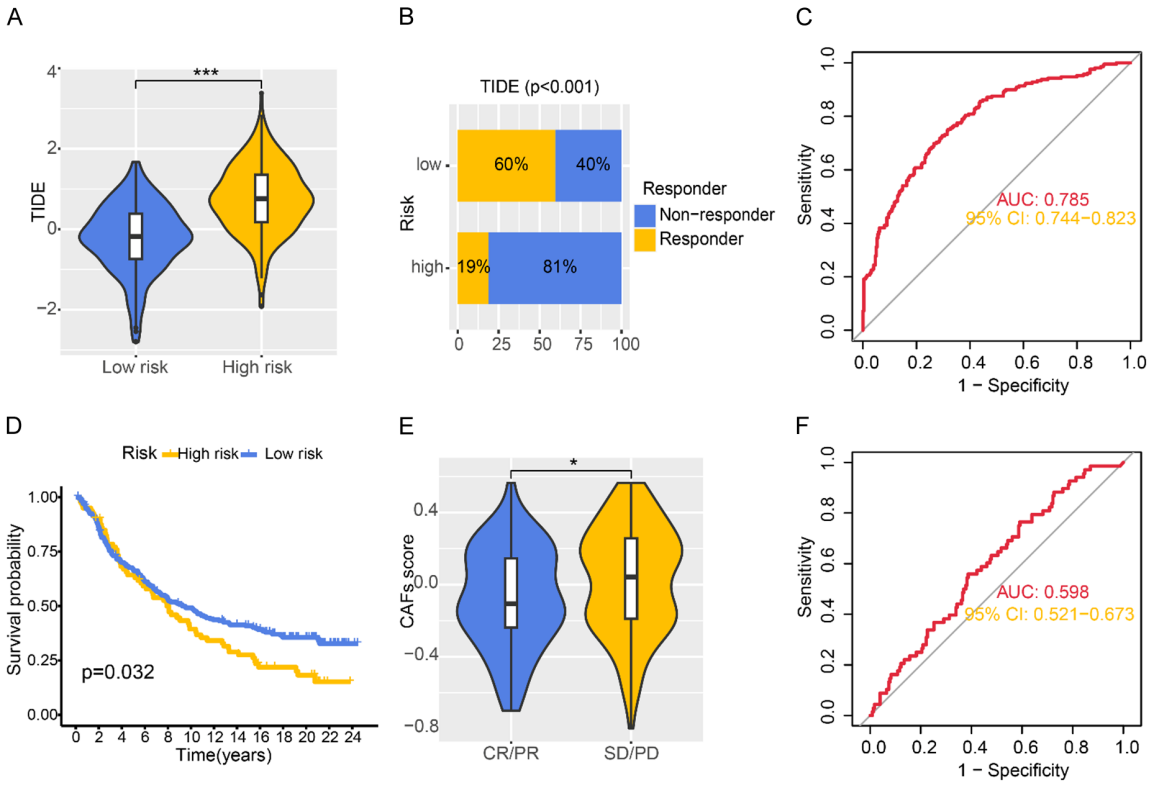

Figure 7. Immunotherapy response in high-CAF and low-CAF groups. A. Comparison of TIDE scores between high-CAF and low-CAF groups in the TCGA-KIRC dataset. B. Distribution of immunotherapy non-responders and responders within the high-CAF and low-CAF groups in the TCGA-KIRC dataset. C. ROC curve analysis for predicting immunotherapy response in the TCGA-KIRC dataset. D. Kaplan-Meier survival curve analysis of the IMvigor210 dataset. E. Differences in CAF scores between SD/PD patients and CR/PR patients in the IMvigor210 dataset. F. ROC curve analysis for predicting immunotherapy response in the IMvigor210 dataset. *P < 0.05; ***P < 0.001. CAFs: cancer-associated fibroblasts; TIDE: Tumor Immune Dysfunction and Exclusion; ROC: Receiver Operating Characteristic; SD/PD: stable disease or progressive disease; CR/PR: complete or partial response; CI: confidence interval.

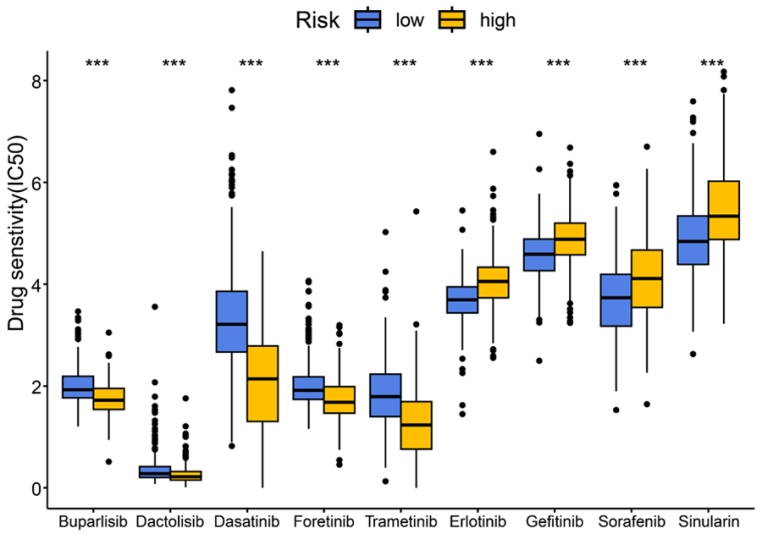

Figure 8. Drug sensitivity analysis in low-CAF and high-CAF groups. ***P < 0.001. CAFs: cancer-associated fibroblasts.

immunotherapy, but the long-term efficacy of this approach is limited because of nonspecific targets [27, 28]. The TME, comprising ECM and stromal cells, significantly influences tumor behaviors, including growth, invasion, and metastasis [29, 30]. CAFs may be activated as a result of HIF-1α accumulation in the TME, which is associated with Von Hippel-Lindau mutations in RCC [31]. Increased density of CAFs enhances tumor cell proliferation, leading to poor prognosis and limited efficiency for targeted therapy in metastatic ccRCC [32]. CAFs enhance the

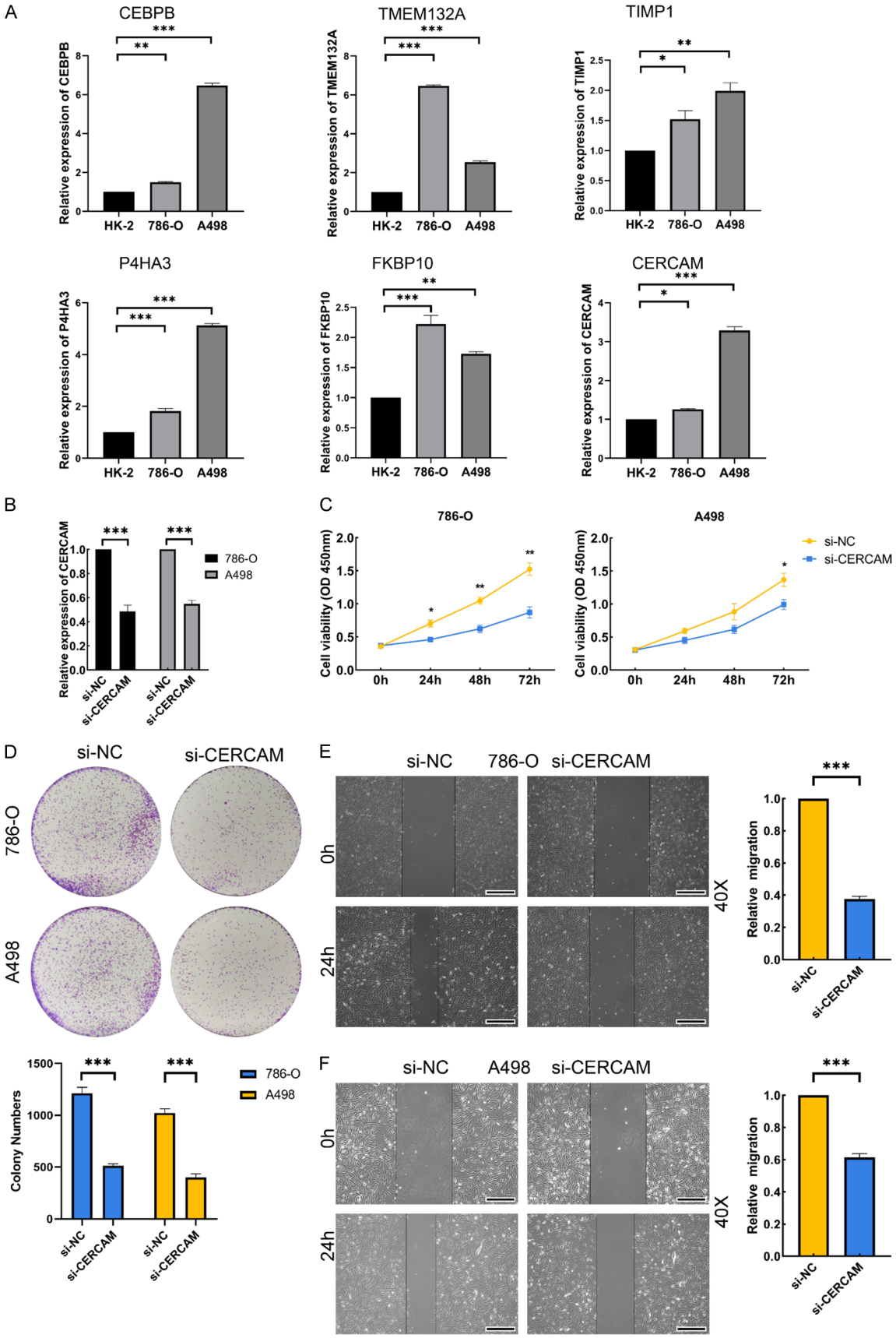
A
CEBPB
TMEM132A
TIMP1
P4HA3
FKBP10
CERCAM
Relative expression of CEBPB
Relative expression of TMEM132A
Relative expression of TIMP1
Relative expression of P4HA3
Relative expression of FKBP10
Relative expression of CERCAM
HK-2
786-O
A498
B
Relative expression of CERCAM
786-O
A498
si-NC
si-CERCAM
C
786-O
A498
Cell viability (OD 450nm)
0h
24h
48h
72h
si-NC
si-CERCAM
D
si-NC
si-CERCAM
786-O
A498
Colony Numbers
E
si-NC
786-O
si-CERCAM
0h
24h
40X
Relative migration
F
si-NC
A498
si-CERCAM
0h
24h
40X
Relative migration

Figure 9. Validation of the CRGs and functional analysis of CERCAM. A. Relative mRNA expression of CERCAM, TMEM132A, TIMP1, P4HA3, FKBP10, and CEBPB in HK-2, 786-O, and A498 cell lines, as determined by RT-qPCR. B. The effects of siRNA-mediated knockdown of CERCAM expression in 786-O and A498 cell lines, as measured by RT-qPCR. C, D. Inhibition of cell proliferation in ccRCC cell lines after CERCAM knockdown, as determined by CCK-8 assays and colony-formation assays. E, F. Inhibition of cell migration in ccRCC cell lines after CERCAM knockdown, as assessed by wound-healing assays. Observation under 40 × magnification and with a 500 μm scale bar. *P < 0.05; **P < 0.01; ***P < 0.001. CRGs: CAF-related genes.

drug resistance of tumor cells by directly secreting soluble factors (including growth factors, cytokines, chemokines, and proteases), reprogramming metabolic processes, inducing epigenetic modifications, and delivering exosomes [33]. Additionally, they impede drug penetration into tumor sites by increasing the rigidity of the ECM and promoting ECM remodeling [14, 34]. Therefore, there is a need to identify relevant biomarkers to improve ccRCC treatment.

In this study, we identified 29 CRGs by successfully integrating the results of bulk RNA-seq and scRNA-seq analyses. This integrative strategy provided a comprehensive perspective, enabling us to precisely pinpoint key CRGs amidst a vast array of genes. Focusing on six key genes - CERCAM, TMEM132A, TIMP1, P4HA3, FKBP10, and CEBPB, - we established and validated models to predict prognosis through univariate Cox and LASSO regression analyses. Previous studies have demonstrated abnormal upregulation of CERCAM in bladder cancer, which notably boosts cell vitality, DNA synthesis, and invasiveness, suggesting that CERCAM may foster bladder cancer proliferation via the PI3K/AKT pathway [35]. CERCAM enhances tumor malignancy and stimulates M2 polarization of macrophages in head and neck squamous cell carcinoma [36]. Therefore, we verified the effect of CERCAM on the malignant biology of ccRCC in vitro by knocking it down in 786-O and A498 cells. The results showed that downregulation of CERCAM inhibited the proliferation and migration of ccRCC cells, consistent with previous findings. TMEM132A is recognized as a novel regulator of the Wnt signaling pathway [37], and its presence can serve as a predictive marker for the overall survival of patients with bladder cancer [38]. In concordance with our observations, dysregulated expression of TIMP1 has been consistently linked to unfavorable outcomes across a spectrum of malignancies, including colon carcinoma, gastric adenocarcinoma, pancreatic neoplasms, papillary thyroid carcinoma, cutaneous melanoma, and mammary carcinoma [39-41]. Under in vitro conditions, targeted silencing of TIMP1 resulted in suppression of the proliferative, migratory, and invasive capacities of RCC cells. Conversely, overexpression of TIMP1 augmented these cellular behaviors [42]. TIMP1 promotes colon cancer proliferation and metastasis through the FAK-PI3K/AKT and MAPK pathways [39]. In co-cultures of CAFs with breast cancer cells, TIMP1 expression was found to be significantly elevated in tumor cells and promoted tumor cell invasion and angiogenesis [43]. CAFs, being the primary source of TIMP1, demonstrated enhanced TIMP1 expression when co-cultured with colon cancer cell lines, which in turn promoted cancer cell migration [44]. P4HA3 has been discovered to play a significant role in activation of the EMT process, thereby promoting the growth, proliferation, and metastasis of tumor cells. This has been observed in various types of cancers, including head and neck squamous cell carcinoma, colon cancer, non-small cell lung cancer, and pituitary adenomas [45]. In vitro, FKBP10 enhances the growth of glioma cells by stimulating the AKT-CREB-PCNA pathway [46]. It also regulates the proliferation, invasion, and migration of gastric cancer cell lines through the PI3K/AKT pathway [47]. In vivo, knockout of FKBP10 inhibited Kras-driven lung tumorigenesis [48]. Upregulation of CEBPB promotes RCC progression through the IL6/STAT3 pathway [49]. CEBPB knockdown has been shown to sensitize nasopharyngeal carcinoma cells to cisplatin by promoting expression of Serine Protease Inhibitor Kazal-type 5, highlighting a potential therapeutic approach to enhance chemotherapy efficacy in nasopharyngeal carcinoma [50]. Altogether, CRGs have been suggested to be detrimental to a variety of tumors. Our findings demonstrate that the CAF score was an independent predictor of survival. Furthermore, we showed that a nomogram based on the CAF score and clinicopathologic features has a robust ability to predict prognosis in ccRCC patients.

Employing GSEA for both KEGG and Hallmark pathways, we gained initial insights into the biological mechanisms underlying the CRG sig-

nature in high-risk patients. Pathways such as EMT, ECM-receptor interactions, hypoxia, and glycolysis displayed significant enrichment and enhanced activity, suggesting their coordinated role in CAF function. Further analysis using the "AUCell" R package confirmed that expression of these pathways was highest in fibroblast cells, implying their central role in the CRG signature. Previous studies indicate that CAFs promote tumor EMT by releasing transforming TGF-β, and concurrent secretion of IL-6 further promotes EMT in various cancers [51, 52]. When tumors grow rapidly, the oxygen supply to tumor cells and associated stromal cells distant from blood vessels diminishes. Under hypoxic conditions, these cells shift to glycolytic metabolism, leading to acidification of the TME. Metabolites produced from glycolysis, such as lactate, can be utilized by tumor cells, thereby promoting tumor growth [53]. Interestingly, the glycolytic phenotype of CAFs is partially maintained through epigenetic reprogramming of HIF-1α and glycolytic enzymes, suggesting potential therapeutic targets for disrupting this metabolic pathway and hindering the contribution of CAFs to tumor progression [54].

Analysis using EPIC highlighted a pronounced increase in tumor infiltration of endothelial cells and macrophages, along with a marked decrease in CD8 T cells and CD4 T cells, within the high-CAF group. CAFs can promote the expression of co-inhibitory markers on CD4 and CD8 T cells [55, 56], contributing to immune evasion and tumor progression [57, 58]. Corroborating these findings, our study found that the CAF score, as well as the proportion of CAF infiltration, was positively correlated with the expression of a majority of immune-checkpoint genes.

Through the application of the TIDE algorithm, we demonstrated the robust capability of the CAF score to predict responses to both anti-PD-1 and anti-CTLA4 therapies in ccRCC. Additionally, validation in the IMvigor210 dataset underscored the exceptional performance of the CAF score in predicting the response to anti-PD-L1 therapy. In previous studies, inhibition of CD36 CAFs enhanced T cell immunotherapy and achieved optimal antitumor efficacy in hepatocellular carcinoma patients [59]. The CAF-specific inhibitor NOX4 has been found to amplify immunotherapy effects by counteracting the CAF-mediated exclusion of CD8 T cells from tumors [60]. Notably, colorectal cancer patients with elevated CAF scores tend to exhibit reduced responsiveness to immunotherapy [61]. Collectively, these insights suggest that the CAF gene signature holds promise as a therapeutic target in ccRCC and presents a novel avenue for predicting personal immunotherapy response in ccRCC patients. On the pharmacological front, our drug sensitivity analysis revealed that patients in the high-CAF group showed increased responsiveness to agents such as buparlisib, dactolisib, dasatinib, foretinib, and trametinib. This may provide new strategies for tailoring targeted treatment regimens to manage ccRCC.

The use of exosomes derived from CAFs as peripheral blood biomarkers for cancer diagnostics, monitoring, and treatment is a rapidly evolving field. These exosomes carry a unique molecular signature, including microRNAs and proteins, that is reflective of the TME [62-64]. In a previous study, candidate biomarkers identified by Lei Liu et al. in gastric cancer tumor tissues exhibited similar expression patterns in serum and exosomes, providing valuable biomarkers for non-invasive diagnosis and prognosis of gastric cancer [65]. Although exosome research was not a part of our study, we posit that the CRGs we identified may serve as pivotal biomarkers within serum exosomes. Should subsequent experiments validate these findings, it would significantly contribute to narrowing the divide between academic research and practical clinical application. However, before these findings can be fully integrated into clinical practice, it is critical to acknowledge and address the limitations of our current research. First, our CRG signature was derived from retrospective data in public databases, emphasizing the need for additional prospective and multicenter ccRCC studies to minimize potential bias. Second, although we validated the relative mRNA expression of the CRGs in cell lines and conducted a functional analysis of CERCAM in vitro, further in vivo validation of our prognostic model is necessary.

Conclusions

We identified CRGs to develop a six-gene model (CERCAM, TMEM132A, TIMP1, P4HA3, FKBP10, and CEBPB) to predict prognosis and therapeutic response in patients with ccRCC. In addition, we analyzed clinicopathologic features, gene functions and pathways,

and immune landscapes to investigate the relationship between the six-gene CAF score and ccRCC. Our findings suggest that this novel gene signature has the potential to improve treatments and make personalized strategies more feasible for ccRCC patients.

Acknowledgements

This study was supported by the Fund of Ningbo Clinical Research Center for Urological Disease (2019A21001), and the Ningbo Top Medical and Health Research Program (No. 2022020203).

Disclosure of conflict of interest

None.

Address correspondence to: Shuben Sun, Department of Urology, The First Affiliated Hospital of Ningbo University, Ningbo 315020, Zhejiang, China. E-mail: nbhappyben@163.com; master@nbdyyy.com

References

[1] Sung H, Ferlay J, Siegel RL, Laversanne M, Soerjomataram I, Jemal A and Bray F. Global cancer statistics 2020: GLOBOCAN estimates of incidence and mortality worldwide for 36 cancers in 185 countries. CA Cancer J Clin 2021; 71: 209-249.

[2] Motzer RJ, Jonasch E, Agarwal N, Alva A, Baine M, Beckermann K, Carlo MI, Choueiri TK, Costello BA, Derweesh IH, Desai A, Ged Y, George S, Gore JL, Haas N, Hancock SL, Kapur P, Kyriakopoulos C, Lam ET, Lara PN, Lau C, Lewis B, Madoff DC, Manley B, Michaelson MD, Mortazavi A, Nandagopal L, Plimack ER, Ponsky L, Ramalingam S, Shuch B, Smith ZL, Sosman J, Dwyer MA, Gurski LA and Motter A. Kidney cancer, version 3.2022, NCCN clinical practice guidelines in oncology. J Natl Compr Canc Netw 2022; 20: 71-90.

[3] Hsieh JJ, Purdue MP, Signoretti S, Swanton C, Albiges L, Schmidinger M, Heng DY, Larkin J and Ficarra V. Renal cell carcinoma. Nat Rev Dis Primers 2017; 3: 17009.

[4] Lalani AA, McGregor BA, Albiges L, Choueiri TK, Motzer R, Powles T, Wood C and Bex A. Systemic treatment of metastatic clear cell renal cell carcinoma in 2018: current paradigms, use of immunotherapy, and future directions. Eur Urol 2019; 75: 100-110.

[5] Barata PC and Rini BI. Treatment of renal cell carcinoma: current status and future directions. CA Cancer J Clin 2017; 67: 507-524.

[6] Kennel KB, Bozlar M, De Valk AF and Greten FR. Cancer-associated fibroblasts in inflammation and antitumor immunity. Clin Cancer Res 2023; 29: 1009-1016.

[7] Gentric G and Mechta-Grigoriou F. Tumor cells and cancer-associated fibroblasts: an updated metabolic perspective. Cancers (Basel) 2021; 13: 399.

[8] Costa A, Kieffer Y, Scholer-Dahirel A, Pelon F, Bourachot B, Cardon M, Sirven P, Magagna I, Fuhrmann L, Bernard C, Bonneau C, Kondratova M, Kuperstein I, Zinovyev A, Givel AM, Parrini MC, Soumelis V, Vincent-Salomon A and Mechta-Grigoriou F. Fibroblast heterogeneity and immunosuppressive environment in human breast cancer. Cancer Cell 2018; 33: 463-479, e410.

[9] Lotti F, Jarrar AM, Pai RK, Hitomi M, Lathia J, Mace A, Gantt GA Jr, Sukhdeo K, DeVecchio J, Vasanji A, Leahy P, Hjelmeland AB, Kalady MF and Rich JN. Chemotherapy activates cancer-associated fibroblasts to maintain colorectal cancer-initiating cells by IL-17A. J Exp Med 2013; 210: 2851-2872.

[10] Jena BC, Rout L, Dey A and Mandal M. Active autophagy in cancer-associated fibroblasts: recent advances in understanding the novel mechanism of tumor progression and therapeutic response. J Cell Physiol 2021; 236: 7887-7902.

[11] Zhou W, Xu G, Wang Y, Xu Z, Liu X, Xu X, Ren G and Tian K. Oxidative stress induced autophagy in cancer associated fibroblast enhances proliferation and metabolism of colorectal cancer cells. Cell Cycle 2017; 16: 73-81.

[12] Yan Y, Chen X, Wang X, Zhao Z, Hu W, Zeng S, Wei J, Yang X, Qian L, Zhou S, Sun L, Gong Z and Xu Z. The effects and the mechanisms of autophagy on the cancer-associated fibroblasts in cancer. J Exp Clin Cancer Res 2019; 38: 171.

[13] Jenkins L, Jungwirth U, Avgustinova A, Iravani M, Mills A, Haider S, Harper J and Isacke CM. Cancer-associated fibroblasts suppress CD8+ T-cell infiltration and confer resistance to immune-checkpoint blockade. Cancer Res 2022; 82: 2904-2917.

[14] Sahai E, Astsaturov I, Cukierman E, DeNardo DG, Egeblad M, Evans RM, Fearon D, Greten FR, Hingorani SR, Hunter T, Hynes RO, Jain RK, Janowitz T, Jorgensen C, Kimmelman AC, Kolonin MG, Maki RG, Powers RS, Pure E, Ramirez DC, Scherz-Shouval R, Sherman MH, Stewart S, Tlsty TD, Tuveson DA, Watt FM, Weaver V, Weeraratna AT and Werb Z. A framework for advancing our understanding of cancer-associated fibroblasts. Nat Rev Cancer 2020; 20: 174-186.

[15] Zhang Z, Liang Z, Li D, Wang L, Chen Y, Liang Y, Jiao W and Niu H. Development of a CAFs-related gene signature to predict survival and drug response in bladder cancer. Hum Cell 2022; 35: 649-664.
[16] Li T, Zhou Z, Xie Z, Fan X, Zhang Y, Zhang Y, Song X and Ruan Y. Identification and validation of cancer-associated fibroblast-related subtypes and the prognosis model of biochemical recurrence in prostate cancer based on single-cell and bulk RNA sequencing. J Cancer Res Clin Oncol 2023; 149: 11379-11395.
[17] Liu B, Chen X, Zhan Y, Wu B and Pan S. Identification of a gene signature for renal cell carcinoma-associated fibroblasts mediating cancer progression and affecting prognosis. Front Cell Dev Biol 2021; 8: 604627.
[18] Chen Z, Zhou L, Liu L, Hou Y, Xiong M, Yang Y, Hu J and Chen K. Single-cell RNA sequencing highlights the role of inflammatory cancer-associated fibroblasts in bladder urothelial carcinoma. Nat Commun 2020; 11: 5077.
[19] Choi JH, Lee BS, Jang JY, Lee YS, Kim HJ, Roh J, Shin YS, Woo HG and Kim CH. Single-cell transcriptome profiling of the stepwise progression of head and neck cancer. Nat Commun 2023; 14: 1055.
[20] Pu W, Shi X, Yu P, Zhang M, Liu Z, Tan L, Han P, Wang Y, Ji D, Gan H, Wei W, Lu Z, Qu N, Hu J, Hu X, Luo Z, Li H, Ji Q, Wang J, Zhang X and Wang YL. Single-cell transcriptomic analysis of the tumor ecosystems underlying initiation and progression of papillary thyroid carcinoma. Nat Commun 2021; 12: 6058.
[21] Hanley CJ, Waise S, Ellis MJ, Lopez MA, Pun WY, Taylor J, Parker R, Kimbley LM, Chee SJ, Shaw EC, West J, Alzetani A, Woo E, Ottensmeier CH, Rose-Zerilli MJJ and Thomas GJ. Single-cell analysis reveals prognostic fibroblast subpopulations linked to molecular and immunological subtypes of lung cancer. Nat Commun 2023; 14: 387.
[22] Sato Y, Yoshizato T, Shiraishi Y, Maekawa S, Okuno Y, Kamura T, Shimamura T, Sato-Otsubo A, Nagae G, Suzuki H, Nagata Y, Yoshida K, Kon A, Suzuki Y, Chiba K, Tanaka H, Niida A, Fujimoto A, Tsunoda T, Morikawa T, Maeda D, Kume H, Sugano S, Fukayama M, Aburatani H, Sanada M, Miyano S, Homma Y and Ogawa S. Integrated molecular analysis of clear-cell renal cell carcinoma. Nat Genet 2013; 45: 860-867.
[23] Leek JT, Johnson WE, Parker HS, Jaffe AE and Storey JD. The sva package for removing batch effects and other unwanted variation in high-throughput experiments. Bioinformatics 2012; 28: 882-883.
[24] Neal JT, Li X, Zhu J, Giangarra V, Grzeskowiak CL, Ju J, Liu IH, Chiou SH, Salahudeen AA, Smith AR, Deutsch BC, Liao L, Zemek AJ, Zhao F, Karlsson K, Schultz LM, Metzner TJ, Nadauld LD, Tseng YY, Alkhairy S, Oh C, Keskula P, Mendoza-Villanueva D, De La Vega FM, Kunz PL, Liao JC, Leppert JT, Sunwoo JB, Sabatti C, Boehm JS, Hahn WC, Zheng GXY, Davis MM and Kuo CJ. Organoid modeling of the tumor immune microenvironment. Cell 2018; 175: 1972-1988, e1916.
[25] Becht E, Giraldo NA, Lacroix L, Buttard B, Elarouci N, Petitprez F, Selves J, Laurent-Puig P, Sautes-Fridman C, Fridman WH and de Reynies A. Estimating the population abundance of tissue-infiltrating immune and stromal cell populations using gene expression. Genome Biol 2016; 17: 218.
[26] Wettersten HI and Weiss RH. Potential biofluid markers and treatment targets for renal cell carcinoma. Nat Rev Urol 2013; 10: 336-344.
[27] Braun DA, Bakouny Z, Hirsch L, Flippot R, Van Allen EM, Wu CJ and Choueiri TK. Beyond conventional immune-checkpoint inhibition - novel immunotherapies for renal cell carcinoma. Nat Rev Clin Oncol 2021; 18: 199-214.
[28] Brown LC, Desai K, Zhang T and Ornstein MC. The immunotherapy landscape in renal cell carcinoma. BioDrugs 2020; 34: 733-748.
[29] Liao Z, Tan ZW, Zhu P and Tan NS. Cancer-associated fibroblasts in tumor microenvironment - accomplices in tumor malignancy. Cell Immunol 2019; 343: 103729.
[30] Wang M, Zhao J, Zhang L, Wei F, Lian Y, Wu Y, Gong Z, Zhang S, Zhou J, Cao K, Li X, Xiong W, Li G, Zeng Z and Guo C. Role of tumor microenvironment in tumorigenesis. J Cancer 2017; 8: 761-773.
[31] Errarte P, Larrinaga G and Lopez JI. The role of cancer-associated fibroblasts in renal cell carcinoma. An example of tumor modulation through tumor/non-tumor cell interactions. J Adv Res 2019; 21: 103-108.
[32] Chakiryan NH, Kimmel GJ, Kim Y, Johnson JO, Clark N, Hajiran A, Chang A, Aydin AM, Zemp L, Katende E, Chahoud J, Ferrall-Fairbanks MC, Spiess PE, Francis N, Fournier M, Dhillon J, Park JY, Wang L, Mule JJ, Altrock PM and Manley BJ. Geospatial cellular distribution of cancer-associated fibroblasts significantly impacts clinical outcomes in metastatic clear cell renal cell carcinoma. Cancers (Basel) 2021; 13: 3743.
[33] Zhang H, Yue X, Chen Z, Liu C, Wu W, Zhang N, Liu Z, Yang L, Jiang Q, Cheng Q, Luo P and Liu G. Define cancer-associated fibroblasts (CAFs) in the tumor microenvironment: new opportunities in cancer immunotherapy and advances in clinical trials. Mol Cancer 2023; 22: 159.
[34] Najafi M, Farhood B and Mortezaee K. Extracellular matrix (ECM) stiffness and degrada-

tion as cancer drivers. J Cell Biochem 2019; 120: 2782-2790.
[35] Zuo Y, Xu X, Chen M and Qi L. The oncogenic role of the cerebral endothelial cell adhesion molecule (CERCAM) in bladder cancer cells in vitro and in vivo. Cancer Med 2021; 10: 4437-4450.
[36] Yang Y, Yan C and Chen XJ. CERCAM is a prognostic biomarker associated with immune infiltration of macrophage M2 polarization in head and neck squamous carcinoma. BMC Oral Health 2023; 23: 724.
[37] Li B and Niswander LA. TMEM132A, a novel Wnt signaling pathway regulator through wntless (WLS) interaction. Front Cell Dev Biol 2020; 8: 599890.
[38] Wu R, Li D, Feng D and Han P. Transmembrane protein 132A (TMEM132A) predicts overall survival for bladder cancer patients. Asian J Surg 2023; 46: 3804-3806.
[39] Song G, Xu S, Zhang H, Wang Y, Xiao C, Jiang T, Wu L, Zhang T, Sun X, Zhong L, Zhou C, Wang Z, Peng Z, Chen J and Wang X. TIMP1 is a prognostic marker for the progression and metastasis of colon cancer through FAK-PI3K/AKT and MAPK pathway. J Exp Clin Cancer Res 2016; 35: 148.
[40] Liu H, Xiang Y, Zong QB, Zhang XY, Wang ZW, Fang SQ, Zhang TC and Liao XH. miR-6745-TIMP1 axis inhibits cell growth and metastasis in gastric cancer. Aging (Albany NY) 2021; 13: 24402-24416.
[41] Tian Z, Ou G, Su M, Li R, Pan L, Lin X, Zou J, Chen S, Li Y, Huang K and Chen Y. TIMP1 derived from pancreatic cancer cells stimulates Schwann cells and promotes the occurrence of perineural invasion. Cancer Lett 2022; 546: 215863.
[42] Shou Y, Liu Y, Xu J, Liu J, Xu T, Tong J, Liu L, Hou Y, Liu D, Yang H, Cheng G and Zhang X. TIMP1 indicates poor prognosis of renal cell carcinoma and accelerates tumorigenesis via EMT signaling pathway. Front Genet 2022; 13: 648134.
[43] Eiro N, Gonzalez L, Martinez-Ordonez A, Fernandez-Garcia B, Gonzalez LO, Cid S, Dominguez F, Perez-Fernandez R and Vizoso FJ. Cancer-associated fibroblasts affect breast cancer cell gene expression, invasion and angiogenesis. Cell Oncol (Dordr) 2018; 41: 369-378.
[44] Nakai N, Hara M, Takahashi H, Shiga K, Hirokawa T, Maeda Y, Yanagita T, Ando N, Takasu K, Suzuki T, Maeda A, Ogawa R, Matsuo Y and Takiguchi S. Cancer cell-induced tissue inhibitor of metalloproteinase-1 secretion by cancer-associated fibroblasts promotes cancer cell migration. Oncol Rep 2022; 47: 112.
[45] Niu X, Ren L, Wang S, Gao D, Ma M, Hu A, Qi H and Zhang S. High prolyl 4-hydroxylase subunit Alpha 3 expression as an independent prognostic biomarker and correlated with immune infiltration in gastric cancer. Front Genet 2022; 13: 952335.
[46] Cai HQ, Zhang MJ, Cheng ZJ, Yu J, Yuan Q, Zhang J, Cai Y, Yang LY, Zhang Y, Hao JJ, Wang MR and Wan JH. FKBP10 promotes proliferation of glioma cells via activating AKT-CREB-PCNA axis. J Biomed Sci 2021; 28: 13.
[47] Wang RG, Zhang D, Zhao CH, Wang QL, Qu H and He QS. FKBP10 functioned as a cancer-promoting factor mediates cell proliferation, invasion, and migration via regulating PI3K signaling pathway in stomach adenocarcinoma. Kaohsiung J Med Sci 2020; 36: 311-317.
[48] Ramadori G, Ioris RM, Villanyi Z, Firnkes R, Panasenko OO, Allen G, Konstantinidou G, Aras E, Brenachot X, Biscotti T, Charollais A, Luchetti M, Bezrukov F, Santinelli A, Samad M, Baldi P, Collart MA and Coppari R. FKBP10 regulates protein translation to sustain lung cancer growth. Cell Rep 2020; 30: 3851-3863, e3856.
[49] Ren Y, Guo W and Qiao B. Abnormal expression of CEBPB promotes the progression of renal cell carcinoma through regulating the generation of IL-6. Heliyon 2023; 9: e20175.
[50] Liu H, Huang Q, Lv Y, Dong Y and Song D. CEBPB knockdown sensitizes nasopharyngeal carcinoma cells to cisplatin by promoting the expression of serine protease inhibitor Kazal-type 5. Anticancer Drugs 2022; 33: e327-e335.
[51] Asif PJ, Longobardi C, Hahne M and Medema JP. The role of cancer-associated fibroblasts in cancer invasion and metastasis. Cancers (Basel) 2021; 13: 4720.
[52] Fiori ME, Di Franco S, Villanova L, Bianca P, Stassi G and De Maria R. Cancer-associated fibroblasts as abettors of tumor progression at the crossroads of EMT and therapy resistance. Mol Cancer 2019; 18: 70.
[53] Petrova V, Annicchiarico-Petruzzelli M, Melino G and Amelio I. The hypoxic tumour microenvironment. Oncogenesis 2018; 7: 10.
[54] Becker LM, O'Connell JT, Vo AP, Cain MP, Tampe D, Bizarro L, Sugimoto H, McGow AK, Asara JM, Lovisa S, McAndrews KM, Zielinski R, Lorenzi PL, Zeisberg M, Raza S, LeBleu VS and Kalluri R. Epigenetic reprogramming of cancer-associated fibroblasts deregulates glucose metabolism and facilitates progression of breast cancer. Cell Rep 2020; 31: 107701.
[55] Gorchs L, Fernandez Moro C, Bankhead P, Kern KP, Sadeak I, Meng Q, Rangelova E and Kaipe H. Human pancreatic carcinoma-associated fibroblasts promote expression of co-inhibitory markers on CD4(+) and CD8(+) T-cells. Front Immunol 2019; 10: 847.

[56] Yu M, Guo G, Huang L, Deng L, Chang CS, Achyut BR, Canning M, Xu N, Arbab AS, Bollag RJ, Rodriguez PC, Mellor AL, Shi H, Munn DH and Cui Y. CD73 on cancer-associated fibroblasts enhanced by the A(2B)-mediated feedforward circuit enforces an immune checkpoint. Nat Commun 2020; 11: 515.

[57] Lakins MA, Ghorani E, Munir H, Martins CP and Shields JD. Cancer-associated fibroblasts induce antigen-specific deletion of CD8 (+) T Cells to protect tumour cells. Nat Commun 2018; 9: 948.

[58] Huang TX, Tan XY, Huang HS, Li YT, Liu BL, Liu KS, Chen X, Chen Z, Guan XY, Zou C and Fu L. Targeting cancer-associated fibroblast-secreted WNT2 restores dendritic cell-mediated antitumour immunity. Gut 2022; 71: 333-344.

[59] Zhu GQ, Tang Z, Huang R, Qu WF, Fang Y, Yang R, Tao CY, Gao J, Wu XL, Sun HX, Zhou YF, Song SS, Ding ZB, Dai Z, Zhou J, Ye D, Wu DJ, Liu WR, Fan J and Shi YH. CD36(+) cancer-associated fibroblasts provide immunosuppressive microenvironment for hepatocellular carcinoma via secretion of macrophage migration inhibitory factor. Cell Discov 2023; 9: 25.

[60] Ford K, Hanley CJ, Mellone M, Szyndralewiez C, Heitz F, Wiesel P, Wood O, Machado M, Lopez MA, Ganesan AP, Wang C, Chakravarthy A, Fenton TR, King EV, Vijayanand P, Ottensmeier CH, Al-Shamkhani A, Savelyeva N and Thomas GJ. NOX4 inhibition potentiates immunotherapy by overcoming cancer-associated fibroblast-mediated CD8 T-cell exclusion from tumors. Cancer Res 2020; 80: 1846-1860.

[61] Zheng H, Liu H, Ge Y and Wang X. Integrated single-cell and bulk RNA sequencing analysis identifies a cancer associated fibroblast-related signature for predicting prognosis and therapeutic responses in colorectal cancer. Cancer Cell Int 2021; 21: 552.

[62] Li C, Teixeira AF, Zhu HJ and Ten Dijke P. Cancer associated-fibroblast-derived exosomes in cancer progression. Mol Cancer 2021; 20: 154.

[63] Liu J, Ren L, Li S, Li W, Zheng X, Yang Y, Fu W, Yi J, Wang J and Du G. The biology, function, and applications of exosomes in cancer. Acta Pharm Sin B 2021; 11: 2783-2797.

[64] Peng L, Wang D, Han Y, Huang T, He X, Wang J and Ou C. Emerging role of cancer-associated fibroblasts-derived exosomes in tumorigenesis. Front Immunol 2022; 12: 795372.

[65] Liu L, Pang H, He Q, Pan B, Sun X, Shan J, Wu L, Wu K, Yao X and Guo Y. A novel strategy to identify candidate diagnostic and prognostic biomarkers for gastric cancer. Cancer Cell Int 2021; 21: 335.